PERIODICO di MINERALOGIA
established in 1930

DIPARTIMENTO DI SCIENZE DELLA TERRA
SAPIENZA UNIVERSITÀ DI ROMA

An International Journal of
Mineralogy, Crystallography, Geochemistry,
Ore Deposits, Petrology, Volcanology
and applied topics on Environment, Archaeometry and Cultural Heritage

The crystal structure of mineral fibres 1. Chrysotile

Simone Pollastri [a,*], Natale Perchiazzi [b], Marco Lezzerini [b], Jasper R. Plaisier [c], Alessandro Cavallo [d], Maria Chiara Dalconi [e], Nicola Bursi Gandolfi [a], Alessandro F. Gualtieri [a]

[a] Department of Chemical and Geological Sciences, University of Modena and Reggio Emilia, Via Campi 103, I-41125 Modena, Italy
[b] Earth Sciences Department, University of Pisa, Via S. Maria 53, I-56126, Pisa, Italy
[c] Elettra-Sincrotrone Trieste S.C.p.A., Strada Statale 14 - km 163,5 in AREA Science Park, 34149 Basovizza, Trieste, Italy
[d] Department of Earth and Environmental Sciences, University Milano-Bicocca, 20126 Milano, Italy
[e] Department of Geosciences, University of Padova, Via G. Gradenigo, 6, 35131 Padova, Italy

ARTICLE INFO

Submitted: May 2016
Accepted: August 2016
Available on line: October 2016

* Corresponding author:
simone.pollastri@unimore.it

DOI: 10.2451/2016PM655

How to cite this article: Pollastri S. et al. (2016) Period. Mineral. 85,249-259

ABSTRACT

This work reports the results of the structural study of three representative chrysotile samples of different provenance (Canadian UICC, and Italian Balangero and Valmalenco). Chemical composition was determined using EMPA and TG data. An innovative wet *cryo-milling* procedure was used to powder the flexible and durable chrysotile fibres. X-ray powder diffraction patterns were collected using both conventional and non-conventional sources. Collected data were used for Rietveld structural refinements and results were compared with available literature data. The three samples display similar structure models, although small differences were detected in the position of the oxygen atoms. Both the structural refinements and spectroscopic investigations confirms that Fe^{2+} and Fe^{3+} atoms in chrysotile are located in the octahedral cavities only, substituting for Mg^{2+}. Regarding the atom coordinates, UICC chrysotile is the closest to the model reported by Falini et al. (2004). About the lattice parameters, the Valmalenco chrysotile is the closest, if compared with the Balangero and UICC, to both the model proposed by Whittaker (1956a,b) and Falini et al. (2004).
This work is intended as a basis for subsequent studies aimed at understanding the toxicity of these mineral fibres.

Keywords: Mineral fibres; chrysotile; Rietveld; iron.

BACKGROUND

The realm of mineral fibres includes asbestos minerals (amphiboles and chrysotile) and fibrous zeolites such as erionite. Many of these natural fibres have a dreadful reputation because they may provoke fatal lung diseases (mainly lung carcinoma and pleural/peritoneal malignant mesothelioma) through inhalation (Becklake et al., 2007). Nevertheless, the mechanisms by which they induce cyto- and geno-toxic damage remain poorly understood mainly because mineral fibres display great chemical variability and molecular arrangements. Moreover, fibre size, surface reactivity, biopersistence and iron oxidation state/coordination number are crucial factors that play a key role in biogeochemical reactions (Fubini and Mollo, 1995; Hardy and Aust, 1995; Donaldson et al., 2010). As a consequence, these minerals have been the subject of intensive multidisciplinary studies in the last two decades, but the investigations were often focused only

on specific cases (e.g. Pacella et al., 2008 for tremolite and Carbone et al., 2013 for erionite). This strategy results in an huge amount of spot data available in the literature, but a general conclusive model explaining the toxicity of mineral fibres still remains a pipe dream.

In this scenario, in order to better understand the nature of the biological interaction mechanisms of the main mineral fibres of socio-economic and industrial importance (chrysotile, amphiboles and erionite) and compare them in a systematic way, a research project entitled "*Sviluppo di un modello generale di interazioni tra fibre minerali e cellule biologiche*", conducted as part of the long term Italian Research Project of National Interest (PRIN) "*Interazione fra minerali e biosfera: conseguenze per l'ambiente e la salute umana*" is being conducted since 2011. This project is specifically focused on mineral fibres and is aimed at the development of a general model of toxicity potential. Considering that there are many mineral fibres (such as zeolites) not yet classified and/or regulated, the model could be very useful to assess their potential degree of toxicity. This could be helpful in preventing new cases of mass exposure as those reported in past for the F-edenite from Biancavilla (Comba et al., 2003) and fibrous erionite from Tuzcöy (Dumortier et al., 2001).

To achieve this goal, it is of fundamental importance to start with a solid base of full mineralogical-structural and microstructural characterization, in order to get a complete picture of the chemical composition and crystal structures of mineral fibres and to detect the presence of impurities that could be relevant for toxicity.

In the frame of this project, the chemical environment of iron within the crystal structure of these fibres has been recently investigated (Pollastri et al., 2015) through a combined X-ray absorption and Mössbauer spectroscopic study. The obtained results indicate that both amphiboles and chrysotile fibres host iron in the octahedral cavities, with Fe^{2+} ions located in the innermost structure positions inside the crystal lattice. Erionite turns out to be a special case since iron seems to be present as octahedrally coordinated Fe^{3+} inside a surface coating of iron-rich phases.

In order to make a step closer to the mineralogical characterization of these samples, the present work is addressed at the determination of impurities and the crystalline structure of chrysotile asbestos samples.

Chrysotile, together with lizardite and antigorite, is a serpentine mineral layer silicate composed of Si-centred tetrahedral (T) sheets in a pseudo-hexagonal network joined to Mg-centered octahedral (O) sheets in units with a 1:1 (TO) ratio (Figure 1a). The general chemical formula of serpentine minerals is $Mg_3(OH)_4Si_2O_5$. Some minor Al^{3+} may substitute for both Si^{4+} and Mg^{2+} in the T and O sheets, respectively; both Fe^{2+} and Fe^{3+} ions, in limited amounts, can replace Mg^{2+} in the O sheet (Stroink et al., 1980; Hardy and Aust, 1995) and Fe^{3+} ions may eventually replace Si^{4+} in the T sheet although this position may preferentially host Al^{3+} (Blaauw et al., 1979; O'Hanley and Dyar, 1998). This cation distribution model has been confirmed by recent spectroscopic investigations (Pollastri et al., 2015) that evidenced only octahedrally coordinated iron in chrysotile samples, with a general prevailing of Fe^{3+} over Fe^{2+}.

The lateral size of an ideal Mg occupied O sheet (b=9.43 Å) is larger than the lateral size of an ideal T Si-occupied sheet (b=9.1 Å); as a result of this misfit and because of the polarity of the TO unit (Bailey, 1988), a differential strain occurs between the two sides of the layer. In chrysotile, the strain is released by rolling the TO layer around the fibril axis (composed of concentrically or spirally curved layers; Figure 1b) to end up with a tubular structure (Yada, 1971). It is important to remark that the cylindrical structure does not completely compensate for the O and T sheet misfit, as only one layer will be at the ideal radius of curvature (namely at 88 Å; Whittaker, 1957) for a perfect match of the sheets along the circumferential direction. Because the layers cannot energetically bear too tight a curvature, the rolls possess hollow cores with a diameter of about 5-8 nm (Cressey et al., 1994) that may be empty or filled with silica or iron-rich amorphous phase. The cross sections of the cylinders can either be circular, spiral, elliptical or deformed (Yada, 1967 and 1971).

The earlier X-ray diffraction studies on chrysotile

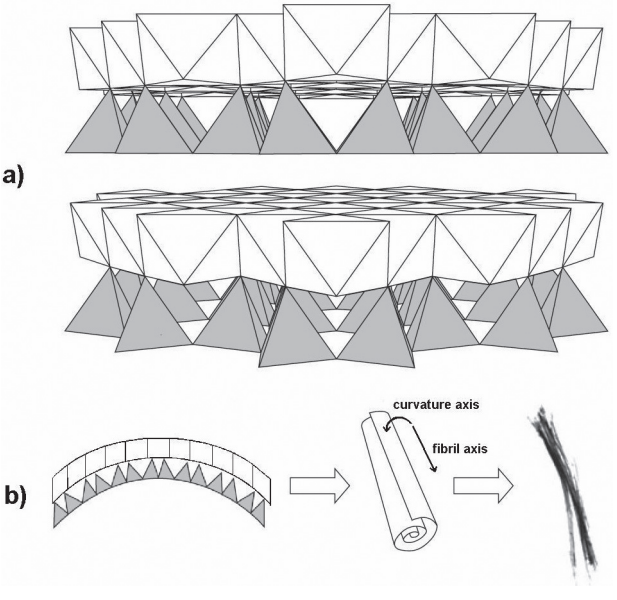

Figure 1. a) Sketch of the structure unit of chrysotile asbestos with a Si-centered tetrahedral sheet joined to a Mg-centered octahedral sheet (b–c crystallographic plane); b) Bending of the TO layers resulting in a rolled papyrus-like microstructure which may compose single chrysotile fibril (from Gualtieri, 2012).

showed a remarkable distortion (curvature) of the unit cell with respect to the Bravaisan monoclinic lattice so that a new theory specially formulated for cylindrical lattices had to be developed (see for example Whittaker, 1954; 1955a,b,c,d; 1956; Devouard and Baronnet, 1995).

Attempts to refine the structure of chrysotile with the Rietveld method have been performed. Falini et al. (2004) have refined nano-chrysotile in the monoclinic space group *Cc*, using the GSAS software (Larson and Von Dreele, 1994). The refined cell parameters were a=5.340(1), b=9.241(1), c=14.689(2) Å, and β=93.66(3)°. The same sample has been the subject of a more robust Rietveld structure refinement using the DIFFaX+ software (Leoni et al., 2004) to empirically reproduce the curved lattice distortions. The best fit was obtained with a model composed of a statistical ensemble of six layers (an ideal and 1/4*b*, 1/3*b*, 1/2*b*, 2/3*b* and 3/4*b* shifted layers) which is a reasonable approximation of the cylindrical stacking with random disorder along the *b* axis. Additional disorder along *a*, reproducing a helical structure, did not improve the fit.

In the present work, three chrysotile samples of different provenance were selected and characterised through Electron Micro-Probe Analysis (EMPA) and X-Ray Powder Diffraction (XRPD) experiments using both conventional sources and synchrotron radiation. The diffraction patterns collected using synchrotron radiation were used for Rietveld structural refinement. The obtained crystal structures, in particular occupancy and position of the iron atoms within the structures (a primary cause of toxicity as it generates active oxygen species, mobilization by chelators and iron-catalyzed reactions; Hardy and Aust, 1995), were compared to the models obtained from previous spectroscopic studies.

MATERIALS AND METHODS

Samples and sample preparation

For the study, three chrysotile samples of different provenance have been selected: 1) UICC standard chrysotile asbestos "B" Canadian (NB #4173-111-1) from Quebec, Canada; 2) chrysotile asbestos from Balangero (Turin, Italy); 3) chrysotile asbestos from Valmalenco (Sondrio, Italy). It is important to note that the UICC chrysotile sample is actually a mixture of fibre from the brands Bells, Carey, Cassair, Flintkote, Johns-Manville, Lake, Normandie and National, proportioned to roughly be representative of Canadian asbestos production at that time. The surface reactivity, chemical environment of iron, thermal behaviour and presence of trace elements in these samples have been already investigated and data are reported in Pollastri et al., (2014; 2015) and Bloise et al., (2016a; 2016b) respectively.

To collect XRPD data suitable for structural analysis, the preparation of finely powdered samples was mandatory. This is rather complicated as conventional grinding techniques such as dry grinding in steel shatterbox (used in Viani et al., 2013) or wet grinding (both mechanical mill and manual in a mortar) have little effect on chrysotile fibres.

For this reasons, we have opted for *cryo-milling* in wet conditions, using a milling machine with a jar and grinding balls in Cr-doped steel equipped with a vessel which injects liquid nitrogen directly on the jar while the machine is running. The milling time was variable depending on the amount of sample and distilled water used, but always in the order of few minutes. This procedure allowed to reduce chrysotile fibres to dimensions suitable for accurate XRPD analyses; the material was subsequently inserted in quartz capillary tubes with a diameter of 0.5 mm.

Experimental and data analysis

Electron Micro Probe Analyses (EMPA) were performed at the Department of Environmental and Territory Sciences and of Earth Sciences of the University of Milano-Bicocca (Italy). A JEOL 8200 Super Probe instrument with W hairpin type filament and minimum accelerating voltage of 30 kV, was used. Analyses were performed on accurately selected fibres so to be highly reliable. The Fe^{3+} concentration was independently calculated using the stoichiometric criteria of the Droop method (Droop, 1987). For the determination of the water content, thermogravimetric and differential scanning calorimetry (TG/DSC) analysis were performed using a Netzsch STA 449 C Jupiter (data and details are reported in Bloise et al., 2016a).

X-Ray Powder Diffraction (XRPD) patterns using a conventional source were collected for the detection of impurities and for crystal structural studies preliminary to the ultimate crystal structure refinements based on synchrotron radiation experimental data. Measurements were conducted at the Department of Geosciences, University of Padova, on capillary samples using a Bragg–Brentano PANalytical X'Pert Pro diffractometer, with a vertical circle Θ–Θ goniometer (240 mm radius), Cu Kα radiation, 40 kV and 40 mA and a PIXcel (solid state pixel technology) detector. Data were collected in focusing transmission geometry, with 1/2° fixed divergence and antiscatter slits and 0.04 rad soller slits. An integrated step scan of the detector of 0.013 °2Θ was used with a counting statistics of 180 s/step from 5 to 80 °2Θ.

High-intensity high-resolution XRPD patterns were collected at the MCX beamline at ELETTRA (Trieste, Italy). Data were collected with an analyzer crystal detector in Debye-Scherrer mode, with either resonant radiation at the absorption K-edge of Fe (≈7 keV, λ 1.7428 Å) and with wavelength off of the absorption edge (≈10 keV, λ 1.2408 Å) in order to investigate the crystal chemistry of iron within the fibres. Quantitative phase analyses were

performed using the Rietveld method (Rietveld, 1969); refinements were accomplished with the GSAS package (Larson and Von Dreele, 1994) and its graphical interface EXPGUI (Toby, 2001).

Rietveld structural refinements were performed with the TOPAS-Academic program (Coelho, 2004). A Pawley refinement (Pawley, 1981) was initially performed to get starting values for background, cell parameters, asymmetry and peak shapes. For the refinements, the starting structural model of Falini et al., (2004) was used. The background was modelled with a 1/*x* function, effective to describe background intensity at low angles due to air scattering, and a 24-terms Chebyschev function. Absorption corrections for intensity and peak position were applied, according to the formulation for a cylindrical sample given by Sabine *et al.* (1998). Lorentzian crystallite size and strain contributions to peak broadening were refined, whereas the strong anisotropic *hkl*-dependent peak broadening was empirically modelled through an 8-term spherical harmonics correction, with a convolution according to the macro *exp_conv_const=(sh1-1) tan (th)* in TOPAS. Soft constraints on Mg-O, Si-O and O-O distances were imposed according to the TOPAS function *penalties_weighting*, initially with high statistic weights, decreased during the final stages of the refinement up to the quite low value of 5.

Table 1. Chemical composition of samples from EMPA analysis. The Fe^{3+} concentration (calculated using the stoichiometric criteria of the Droop method) differs from the accurate Fe^{2+}/Fe^{3+} ratios obtained from spectroscopic investigations (Pollastri et al., 2015); this is probably due to the fact that the Droop approach is not accurate in samples with low iron content (like chrysotile), and Fe^{3+} percentages were greatly underestimated. Reported chemical compositions are mean values of several analyses carried out on various fibres (not less than 10).

Oxides wt%	Chrysotile UICC	Chrysotile Balangero	Chrysotile Valmalenco
SiO_2	42.5 (3)	40.6 (5)	42.5 (2)
TiO_2	0.01 (2)	0.01 (2)	0.06 (5)
Al_2O_3	0.2 (1)	2.4 (6)	0.20 (8)
Cr_2O_3	0.05 (4)	0.2 (3)	0.08 (8)
MnO	0.05 (4)	0.06 (4)	0.06 (4)
MgO	41.9 (2)	39.8 (6)	41.6 (2)
CaO	0.01 (1)	0.02 (2)	0.09 (6)
Na_2O	0.013 (9)	0.012 (9)	0.02 (1)
K_2O	0.004 (5)	0.003 (7)	0.05 (9)
NiO	0.06 (4)	0.05 (7)	0.2 (1)
Fe_2O_3	0.2 (2)	0.4 (3)	0.0 (2)
FeO	1.4 (3)	2.5 (5)	1.4 (1)
Total	86.4	86.1	86.3

RESULTS

The chemical compositions of samples, obtained from EMPA analysis, are reported in Table 1. These data, together with the water content from TG/DSC analysis (Bloise et al., 2015) allowed the calculation of the chemical formula of samples presented in Table 2.

Concerning the XRPD experiments, a comparison of the patterns collected using conventional diffractometer is reported in Figure 2; although samples are similar, differences can be noticed in the relative peak intensities. From the convergence of EMPA observations and qualitative/quantitative phase analysis on the XRPD data, impurities (all less than 1 wt%) were detected for each sample and reported in Table 3.

In Figures 3, 4 and 5, the fit obtained through Rietveld structural refinements (on the data collected at 10 keV) are reported for each sample. The combined refinements of both the data collected at 7 and 10 keV allowed to obtain unit cell parameters, thermal parameters, spatial group and anion-cation distances, reported in Tables 4-10.

DISCUSSION

Before discussing the details of the structural refinements, it should be remarked that the reported structural models bear an intrinsic approximation because

Table 2. Chemical formula of samples determined using EMPA and TG data.

Chrysotile	Crystal-chemical formulae
UICC[1]	$(Mg_{5.93}Fe^{2+}_{0.04}Al_{0.02}Fe^{3+}_{0.08})_{6.07}Si_{4.03}O_{10}(OH)_{7.66}$
Balangero[1]	$(Mg_{5.81}Fe^{2+}_{0.15}Al_{0.27}Fe^{3+}_{0.09}Cr_{0.01})_{6.33}Si_{3.97}O_{10}(OH)_{7.11}$
Valmalenco[1]	$(Mg_{5.85}Fe^{2+}_{0.06}Al_{0.02}Fe^{3+}_{0.05}Ni_{0.01})_{5.99}Si_{4.01}O_{10}(OH)_{7.86}$

[1]The Fe^{2+}/Fe^{3+} ratio is referred to the accurate result obtained from XAS and ^{57}Fe Mössbauer analyses.

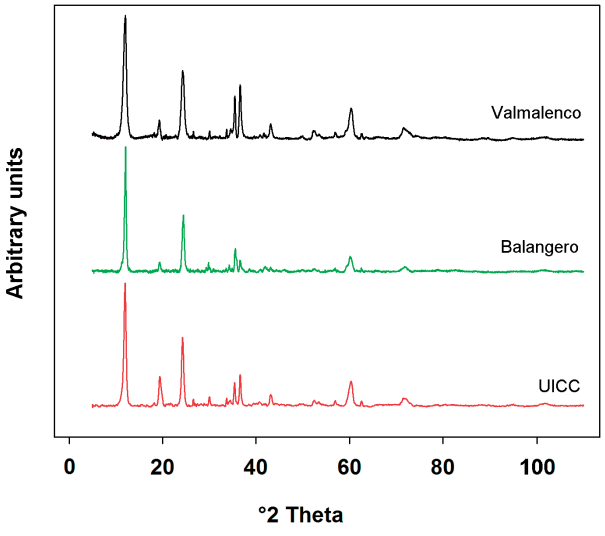

Figure 2. Comparison of (background subtracted) XRPD patterns of the three investigated samples collected using the conventional diffractometer (intensities were normalized with respect to the major reflection).

of the distortion of the unit cell due to the cylindrical lattice. The anisotropic peak broadening due to the cylindrical distortion has been empirically accounted for using an 8-term spherical harmonics correction available in TOPAS (see the "materials and methods" heading). This empirical but robust model was capable to successfully reproduce the strong anisotropic *hkl*-dependent peak broadening displayed by all the chrysotile samples. The understanding of the differences in terms of lattice distortion and structure disorder will be the subject of a dedicated TEM study, presently in progress.

It is well known that chrysotile may display different proportions of monoclinic and orthorhombic polymorphs. A careful qualitative analysis of the powder patterns first, and the successful selection of the monoclinic structure model during the Rietveld refinement, testify that the three samples are mainly composed of clinochrysotile polymorph. The presence of the diagnostic peaks of orthochrysotile at 34.2 and 38.6 °2θ (Cu Kα) corresponding to the *201* (d=2.62 Å) and *203* (d=2.33 Å) reflections (Bailey, 1988), respectively has been carefully inspected. Only the sample from Balangero

Table 3 - Mineral impurities detected in the investigated samples. Magnetite-maghemite impurities were accurately detected in the previously performed spectroscopic investigations (Pollastri et al., 2015).

Chrysotile	Impurities
UICC	brucite, calcite, clinochlore, dolomite, magnetite, microcline, pyroaurite, talc, quartz
Balangero	antigorite, balangeroite, calcite, clinochlore, diopside, dolomite, magnetite, microcline, plagioclase, talc
Valmalenco	calcite, forsterite, magnetite, quartz, lizardite/antigorite, clinochlore

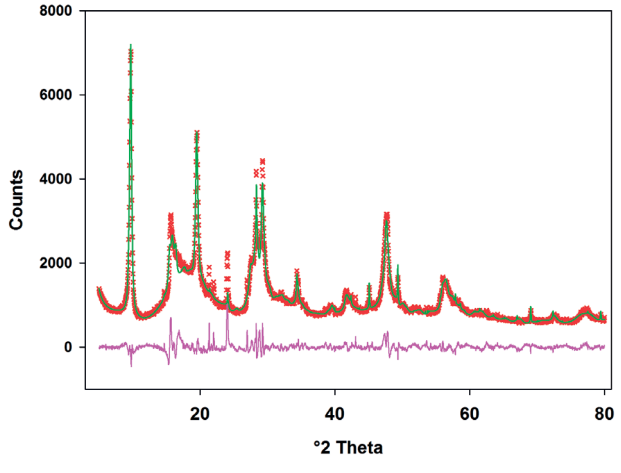

Figure 3. Rietveld refinement of data collected at 10keV of chrysotile UICC. Observed (crosses), calculated (continuous line), and difference (bottom line) curves are reported.

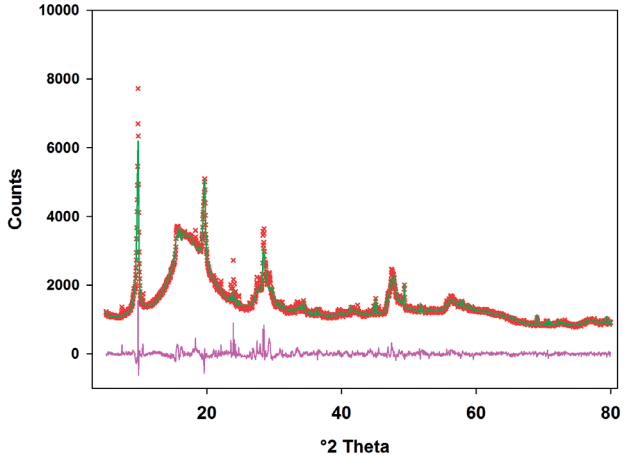

Figure 4. Rietveld refinement of data collected at 10keV of chrysotile Balangero. Observed (crosses), calculated (continuous line), and difference (bottom line) curves are reported.

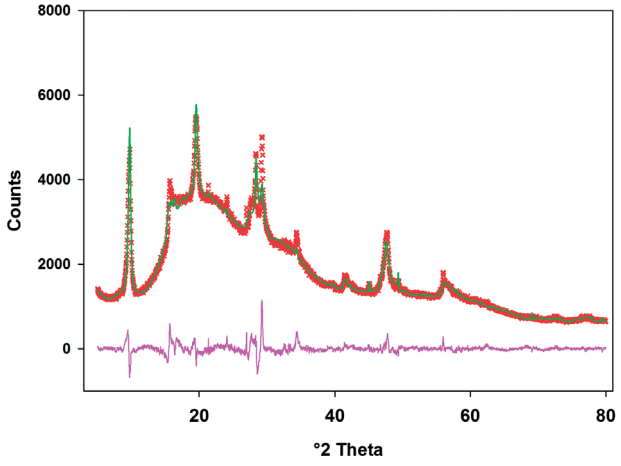

Figure 5. Rietveld refinement of data collected at 10keV of chrysotile Valmalenco. Observed (crosses), calculated (continuous line), and difference (bottom line) curves are reported.

Table 4. Unit cell parameters and agreement factors of the refinement for investigated chrysotile samples.

	UICC	Balangero	Valmalenco
a (Å)	5.354 (3)	5.394 (3)	5.348 (3)
b (Å)	9.155 (6)	9.204 (5)	9.23 (1)
c (Å)	14.735 (5)	14.553 (3)	14.717 (7)
β (°)	93.60 (4)	94.10 (8)	93.96 (6)
sp. gr.	*Cc*	*Cc*	*Cc*
R_{wp}	5.805 %	3.870 %	4.220 %
R_p	3.994 %	2.716 %	2.946 %
χ^2	2.001	1.773	2.107

shows such minor reflections indicating the possible coexistence of clinochrysotile and orthochrysotile. The fraction of the latter is estimated well below 5 wt%. The structural models are also biased by the possible presence of minor intergrowth of serpentine polymorphs lizardite and antigorite detected in the samples from Balangero and Valmalenco.

The obtained structures of chrysotile samples are similar with each other. Small differences (0.03-0.06 Å) were observed in the *x, y* coordinates of the oxygen atoms O1 and O2 between UICC and Balangero/Valmalenco specimens. As stated above, lattice distortion due to the cylindrical curvature may be a reason for such structural differences. As a matter of fact, there are differences in the rolling mode of the fibrils for the investigated chrysotile samples: cylindrical spiral for the UICC sample (Yada, 1967) and cylindrical circular (concentric) for the Balangero chrysotile (Mellini, 1986). Whittaker (1953) already observed that one of the effects of the circular stacking arrangement is the displacement of one of the basal oxygen atom from its ideal position parallel to the cylinder axis.

With respect to literature data, a crystal structure of

Table 5. Final atomic coordinates, occupancies and atomic displacement parameters (Å^2) for UICC chrysotile.

site	*x/a*	*y/b*	*z/c*	occupancy	U_{iso}
M(1)	0.9237(16)	0.1370(8)	0.2495(6)	$Mg_{0.96}Fe_{0.04}$	0.004(4)
M(2)	0.410(2)	0.2953(10)	0.2456(7)	$Mg_{0.96}Fe_{0.04}$	0.004(4)
M(3)	0.8992(15)	0.4505(8)	0.2137(6)	$Mg_{0.96}Fe_{0.04}$	0.004(4)
T(1)	0.0433(10)	0.3016(6)	0.0485(3)	$Si_{1.00}$	0.006(4)
T(2)	0.5225(10)	0.4740(6)	0.0462(3)	$Si_{1.00}$	0.006(4)
O(1)	0.0406(17)	0.1385(9)	0.0028(5)	$O_{1.00}$	0.008(4)
O(2)	0.2583(8)	0.4018(9)	0.0029(5)	$O_{1.00}$	0.008(4)
O(3)	0.7706(9)	0.3795(10)	0.0231(5)	$O_{1.00}$	0.008(4)
O(4)	0.0999(14)	0.2799(8)	0.1587(4)	$O_{1.00}$	0.008(4)
O(5)	0.5105(13)	0.4755(9)	0.1580(4)	$O_{1.00}$	0.008(4)
OH(1)	0.759(2)	0.3127(15)	0.3155(12)	$O_{1.00}$	0.008(4)
OH(2)	0.2857(18)	0.1062(14)	0.3099(6)	$O_{1.00}$	0.008(4)
OH(3)	0.573(2)	0.1241(16)	0.1760(6)	$O_{1.00}$	0.008(4)
OH(4)	0.226(2)	0.4564(15)	0.2977(8)	$O_{1.00}$	0.008(4)

clino-chrysotile has been refined by Whittaker (1956a) but a direct comparison of the atomic coordinates is difficult because a monoclinic space group *C*2 has been used; nevertheless, a significant difference can be observed in the length of the Si-O bond, being 1.64 Å for all our samples and 1.71 Å that of Whittaker (1956a).

Although there is a general agreement between the coordinates of our structure models and those reported by Falini et al. (2004), a slight mismatch exists with the Balangero and Valmalenco samples: a shift of about 0.12 Å is observed for the *y* coordinate of the O2 oxygen and a shift of about 0.09 Å is observed for the *x* coordinate of

Table 6. Selected distances (Å) for octahedral (M) and tetrahedral (T) sites in UICC chrysotile.

M(1)	- O5	2.074(11)	M(2)	- OH4	1.957(17)	M(3)	- OH3	1.940(16)
	- OH2	2.101(13)		- O4	2.038(12)		- OH4	2.079(14)
	- OH1	2.104(17)		- OH1	2.081(17)		- O4	2.088(11)
	- OH4	2.110(16)		- OH3	2.093(17)		- OH2	2.126(14)
	- OH3	2.114(14)		- OH2	2.102(15)		- OH1	2.133(18)
	- O4	2.133(11)		- O5	2.183(12)		- O5	2.201(11)
	average	2.106		average	2.076		average	2.0945
			T(1)	- O1	1.638(9)	T(2)	- O3	1.639(8)
				- O4	1.645(7)		- O1	1.642(9)
				- O3	1.647(8)		- O2	1.652(7)
				- O2	1.648(8)		- O5	1.653(7)
				average	1.6444		average	1.6464

Table 7. Final atomic coordinates, occupancies and atomic displacement parameters (Å^2) for Balangero chrysotile.

site	*x/a*	*y/b*	*z/c*	occupancy	U_{iso}
M(1)	0.9178(16)	0.1414(8)	0.2474(7)	$Mg_{0.92}Fe_{0.08}$	0.012(4)
M(2)	0.4241(15)	0.3078(9)	0.2495(7)	$Mg_{0.92}Fe_{0.08}$	0.012(4)
M(3)	0.8894(14)	0.4527(7)	0.2111(6)	$Mg_{0.92}Fe_{0.08}$	0.012(4)
T(1)	0.0461(11)	0.2791(6)	0.0466(3)	$Si_{1.00}$	0.016(6)
T(2)	0.5280(10)	0.4519(6)	0.0461(3)	$Si_{1.00}$	0.016(6)
O(1)	0.017(3)	0.1143(7)	0.0000(5)	$O_{1.00}$	0.019(5)
O(2)	0.2892(12)	0.3558(12)	0.0035(5)	$O_{1.00}$	0.019(5)
O(3)	0.7862(13)	0.3677(14)	0.0219(6)	$O_{1.00}$	0.019(5)
O(4)	0.1028(13)	0.2761(8)	0.1593(4)	$O_{1.00}$	0.019(5)
O(5)	0.5056(14)	0.4723(10)	0.1573(4)	$O_{1.00}$	0.019(5)
OH(1)	0.772(2)	0.3191(15)	0.3226(13)	$O_{1.00}$	0.019(5)
OH(2)	0.2778(18)	0.1156(13)	0.3036(7)	$O_{1.00}$	0.019(5)
OH(3)	0.5744(18)	0.1405(12)	0.1714(6)	$O_{1.00}$	0.019(5)
OH(4)	0.211(2)	0.4752(13)	0.3012(9)	$O_{1.00}$	0.019(5)

Table 8. Selected distances (in Å) for octahedral (M) and tetrahedral (T) sites for Balangero chrysotile.

M(1)	- OH2	2.066(13)	M(2)	- O5	2.090(12)	M(3)	- OH3	2.097(13)
	- OH4	2.079(15)		- OH1	2.094(16)		- OH4	2.108(14)
	- OH3	2.088(13)		- OH4	2.095(15)		- OH2	2.130(14)
	- O4	2.089(11)		- OH3	2.110(14)		- O4	2.159(10)
	- O5	2.111(12)		- O4	2.118(11)		- O5	2.167(10)
	- OH1	2.148(18)		- OH2	2.112(15)		- OH1	2.167(19)
	average	2.097		average	2.103		average	2.138
			T(1)	- O3	1.639(11)	T(2)	- O1	1.638(9)
				- O4	1.647(8)		- O5	1.643(8)
				- O2	1.652(10)		- O3	1.654(11)
				- O1	1.665(9)		- O2	1.647(9)
				average	1.651		average	1.645

Table 9. Final atomic coordinates, occupancies and atomic displacement parameters (Å^2) for Valmalenco chrysotile.

site	*x/a*	*y/b*	*z/c*	occupancy	U_{iso}
M(1)	0.917(2)	0.1390(11)	0.2470(8)	$Mg_{0.96}Fe_{0.04}$	0.005(6)
M(2)	0.392(2)	0.3039(12)	0.2498(9)	$Mg_{0.96}Fe_{0.04}$	0.005(6)
M(3)	0.8849(19)	0.4509(10)	0.2089(7)	$Mg_{0.96}Fe_{0.04}$	0.005(6)
T(1)	0.0356(14)	0.2851(7)	0.0449(4)	$Si_{1.00}$	0.007(7)
T(2)	0.5193(12)	0.4613(7)	0.0444(4)	$Si_{1.00}$	0.007(7)
O(1)	-0.019(3)	0.1236(12)	0.0000(7)	$O_{1.00}$	0.008(6)
O(2)	0.2865(3)	0.3557(12)	0.0038(6)	$O_{1.00}$	0.008(6)
O(3)	0.7876(14)	0.3877(14)	0.0212(9)	$O_{1.00}$	0.008(6)
O(4)	0.0869(17)	0.2753(10)	0.1564(6)	$O_{1.00}$	0.008(6)
O(5)	0.4948(17)	0.4715(14)	0.1557(5)	$O_{1.00}$	0.008(6)
OH(1)	0.752(3)	0.3151(19)	0.3102(17)	$O_{1.00}$	0.008(6)
OH(2)	0.282(3)	0.1064(17)	0.3042(8)	$O_{1.00}$	0.008(6)
OH(3)	0.567(2)	0.1412(15)	0.1726(7)	$O_{1.00}$	0.008(6)
OH(4)	0.197(3)	0.4756(15)	0.2996(10)	$O_{1.00}$	0.008(6)

the O1 oxygen atom.

Regarding the atomic coordinates, the calculated structure model of UICC chrysotile turns out to be the closest to the model of Falini et al. (2004). Concerning the lattice parameters, the sample of Valmalenco is the closest to both the structures of Whittaker (1956 a,b,c) and that of Falini et al. (2004). It is important to remark that only our structure models take into account the presence of Fe atoms in place of Mg in the octahedral layer. The cationic site occupancies are in agreement with the chemical compositions reported in Table 1.

Concerning the Fe-O distances, a direct comparison with the data from EXAFS refinements is precluded both by the presence of impurities with octahedrally coordinated iron

Table 10. Selected distances (in Å) for octahedral (M) and tetrahedral (T) sites for Valmalenco chrysotile.

M(1)	- O4	2.087(15)	M(2)	- OH4	2.061(19)	M(3)	- OH4	2.076(18)
	- OH4	2.094(18)		- OH1	2.07(2)		- OH3	2.094(16)
	- OH2	2.094(17)		- O4	2.075(15)		- OH2	2.108(17)
	- OH1	2.10(2)		- OH2	2.093(19)		- OH1	2.11(2)
	- OH3	2.103(15)		- OH3	2.137(18)		- O4	2.124(13)
	- O5	2.110(16)		- O5	2.173(17)		- O5	2.185(13)
	average	2.0973		average	2.101		average	2.116
			T(1)	- O2	1.644(11)	T(2)	- O2	1.642(12)
				- O3	1.647(12)		- O3	1.645(11)
				- O4	1.648(11)		- O5	1.654(10)
				- O1	1.649(13)		- O2	1.660(11)
				average	1.647		average	1.650

Table 11. Mean Fe-O distances (Å) as obtained from EXAFS refinements (raw and corrected data) and Rietveld structural refinements (average of the M(1)-O, M(2)-O and M(3)-O distances).

Chrysotile	EXAFS	EXAFS corr.	XRPD
UICC	2.028 (6)	2.036	2.092 (15)
Balangero	2.054 (4)	2.064	2.11 (2)
Valmalenco	2.033 (3)	2.036	2.105 (11)

in the samples (magnetite-maghemite), and because the distances obtained from Rietveld structural refinements are referred to the whole octahedral M sites, which contains mainly Mg. Despite this, as showed in Table 11, there is a correspondence between the two data sets and the differences between the individual samples are reflected. We have also tried to empirically correct the EXAFS data by considering the Fe-O distances of octahedrally coordinated Fe in ideal magnetite-maghemite (2.02 Å; Disch, 2010) and subtracting this contribution in relation to the percentage of iron belonging to these impurities with respect to the total iron. The obtained values (column 2 in Table 11) are actually closer to that from Rietveld structural refinements. In any case, it is important to note that the distances from structure refinements are invariably greater than those determined by EXAFS, and this is probably related to the prevailing presence of Mg in the octahedral sites (the expected distance of octahedrally coordinated Mg-O is 2.12 Å, longer than that of octahedral Fe^{3+}/Fe^{2+}, in equal percentages, of about 2.077 Å; Pollastri et al., 2015).

CONCLUSIONS

In this work, the crystal structure of three reference chrysotile samples of different provenance (standard UICC, Balangero and Valmalenco) were determined from the Rietveld analysis using X-ray synchrotron powder diffraction data. The chemical composition was determined using EMPA and TG data. Samples were reduced to powder using a *cryo-milling* procedure in wet mode. XRPD patterns were collected using both conventional and non-conventional sources. The results of the Rietveld structural refinements were compared with the literature and spectroscopic data. The three samples display similar crystal structures, although small differences were detected in the O1 and O2 oxygen atoms coordinates.

Regarding the atom coordinates, chrysotile UICC is similar to that of Falini et al. (2004), whereas considering the lattice parameters, the chrysotile from Valmalenco is similar to both that of Whittaker (1956a,b) and of Falini et al. (2004). From the convergence of structural refinements and previously conducted spectroscopic investigations we can confirm that, in chrysotile, Fe^{2+} and Fe^{3+} atoms seem to be located only in octahedral cavities, in substitution of Mg^{2+}.

ACKNOWLEDGMENTS

This research was conducted within the research project "*Sviluppo di un modello generale di interazioni tra fibre minerali e cellule biologiche*", a part of the comprehensive granted long term Italian Research Project of National Interest (PRIN 2011) entitled "*Interazione fra minerali e biosfera: conseguenze per l'ambiente e la salute umana*". This work was financially supported by the University of Pisa through the project P.R.A. 2016 "*Ruolo di zone di taglio nella costruzione degli orogeni: case histories da catene orogenetiche*". Synchrotron XRPD patterns were collected at the MCX beamline (ELETTRA, Trieste, Italy) during the experiment 20150053 (July 2015). We want to thank Prof. Stefano Gialanella, of the University of Trento, for the lending of the crio-milling machine.

REFERENCES

Bailey S.W. (1988) Hydrous phyllosilicates (exclusive of micas), Reviews in Mineralogy, Mineralogical Society of America 19, pp 725.

Becklake M.R., Bagatin E., Neder J.A. (2007). Asbestos-related diseases of the lungs and pleura: uses, trends and management over the last century [State of the Art Series. Occupational lung disease in high-and low-income countries, Edited by M. Chan-Yeung. Number 3 in the series]. The International Journal of Tuberculosis and Lung Disease 11, 356-369.

Blaauw C., Stroink G., Leiper W., Zentilli M. (1979) Mössbauer analysis of some canadian chrysotiles, Canadian Mineralogist 17, 713-717.

Bloise A., Catalano M., Barrese E., Gualtieri A.F., Gandolfi N.B., Capella S., Belluso E. (2016a) TG/DSC study of the thermal behaviour of hazardous mineral fibres. Journal of Thermal Analysis and Calorimetry, 123, 2225-2239.

Bloise A., Barca D., Gualtieri A.F., Pollastri S., Belluso E. (2016b) Trace elements in hazardous mineral fibres. Environmental Pollution 216, 314-323.

Carbone M., Yang H., Pass H.I., Krausz T., Testa J.R., Gaudino G. (2013) BAP1 and cancer. Nature Reviews Cancer 13, 153-159.

Coelho A.A. (2004) Topas-Academic. A Computer Programme for Rietveld Analysis.

Comba P., Gianfagna A., Paoletti L. (2003) Pleural mesothelioma cases in Biancavilla are related to a new fluoro-edenite fibrous amphibole. Archives of Environmental Health: An International Journal 58, 229-232.

Cressey B.A., Cressey G., Cernik R.J. (1994) Structural variations in chrysotile asbestos fibers revealed by synchrotron X-ray diffraction and high resolution transmission electron microscopy. Canadian Mineralogist 32, 257-270.

Devouard B. and Baronnet A. (1995) Axial diffraction of curved lattices: geometrical and numerical modeling. Application to chrysotile. European Journal of Mineralogy 7, 835-846.

Disch S. (2010). The spin structure of magnetic nanoparticles and in magnetic nanostructures (Vol. 21). Forschungszentrum Jülich.

Donaldson K., Murphy F.A., Duffin R., Poland C.A. (2010) Asbestos, carbon nanotubes and the pleural mesothelium: a review of the hypothesis regarding the role of long fibre retention in the parietal pleura, inflammation and mesothelioma. Particle and Fibre Toxicology 7, 1-17.

Droop G.T.R. (1987) A general equation for estimating Fe^{3+} concentrations in ferromagnesian silicates and oxides from microprobe analyses, using stoichiometric criteria. Mineralogical Magazine 51, 431-435.

Dumortier P., Coplü L., Broucke I., Emri S., Selcuk T., De Maertelaer V., De Vuist P., Baris I. (2001) Erionite bodies and fibres in bronchoalveolar lavage fluid (BALF) of residents from Tuzköy, Cappadocia, Turkey. Occupational and Environmental Medicine 58, 261-266.

Falini G., Foresti E., Gazzano M., Gualtieri A.F., Leoni M., Lesci I. G., Roveri N. (2004) Tubular-Shaped Stoichiometric Chrysotile Nanocrystals. Chemistry-A European Journal 10, 3043-3049.

Fubini B., and Mollo L. (1995) Role of iron in the reactivity of mineral fibers. Toxicology Letters 82, 951-960.

Gualtieri A.F. (2012) Mineral fibre-based building materials and their health hazards. In Pacheco-Torgal F., Jalali S., and Fucic A. (Eds.). Toxicity of building materials. Elsevier, pp. 166-195. Woodhead, Cambridge.

Hardy J.A. and Aust A.E. (1995) Iron in asbestos chemistry and carcinogenicity. Chemical Reviews 95, 97-118.

Larson A.C. and Von Dreele R.B. (1994) Generalized Structure Analysis System. Los Alamos National Lab, New Mexico, LAUR 86-748.

Leoni M., Gualtieri A.F., Roveri N. (2004) Simultaneous refinement of structure and microstructure of layered materials. Journal of applied crystallography 37, 166-173.

Mellini M. (1986) Chrysotile and polygonal serpentine from the Balangero serpentinite. Mineralogical Magazine 50, 301-306.

O'Hanley D.S., and Dyar M.D. (1998) The composition of chrysotile and its relationship with lizardite. Canadian Mineralogist 36, 727-740.

Pacella A., Andreozzi, G.B., Ballirano P., Gianfagna A. (2008) Crystal chemical and structural characterization of fibrous tremolite from Ala di Stura (Lanzo Valley, Italy). Periodico di Mineralogia 77, 51-62.

Pawley G.S. (1981) Unit-cell refinement from powder diffraction scans. Journal of Applied Crystallography 14, 357-361.

Pollastri S., Gualtieri A.F., Gualtieri M.L., Hanuskova M., Cavallo A., Gaudino G. (2014) The zeta potential of mineral fibres. Journal of Hazardous Materials 276, 469-479.

Pollastri S., D'Acapito F., Trapananti A., Colantoni I., Andreozzi G.B., Gualtieri A.F. (2015) The chemical environment of iron in mineral fibres. A combined X-ray absorption and Mössbauer spectroscopic study. Journal of Hazardous Materials 298, 282-293.

Rietveld H.M. (1969) A profile refinement method for nuclear and magnetic structures. Journal of Applied Crystallography 2, 65-71.

Sabine T.M., Hunter B.A., Sabine W.R., Ball C.J. (1998) Analytical expressions for the transmission factor and peak shift in absorbing cylindrical specimens. Journal of Applied Crystallography 31, 47-51.

Stroink G., Blaauw C., White C.G., Leiper W. (1980) Mössbauer characteristics of UICC standard reference asbestos samples. Canadian Mineralogist 18, 285-290.

Toby B.H. (2001) EXPGUI, a graphical user interface for GSAS. Journal of applied crystallography 34, 210-213.

Viani A., Gualtieri A.F., Pollastri S., Rinaudo C., Croce A., Urso G. (2013) Crystal chemistry of the high temperature product of transformation of cement-asbestos. Journal of Hazardous

Materials 248, 69-80.
Whittaker E.J.W. (1953) The structure of chrysotile. Acta Crystallographica 6, 747-748.
Whittaker E.J.W. (1954) The diffraction of X-rays by a cylindrical lattice I. Acta Crystallographica 7, 827-832.
Whittaker E.J.W. (1955a) The diffraction of X-rays by a cylindrical lattice II. Acta Crystallographica 8, 261-265.
Whittaker E.J.W. (1955b) The diffraction of X-rays by a cylindrical lattice III. Acta Crystallographica 8, 265-271.
Whittaker E.J.W. (1955c) A classification of cylindrical lattices. Acta Crystallographica 8, 571-574.
Whittaker E.J.W. (1955d) The diffraction of X-rays by a cylindrical lattice IV. Acta Crystallographica, 8, 726-729.
Whittaker E.J.W. (1956a) The structure of chrysotile II. Clinochrysotile. Acta Crystallographica 9, 855-862.
Whittaker E.J.W. (1956b) The structure of chrysotile III. Orthochrysotile. Acta Crystallographica 9, 862-864.
Whittaker E.J.W. (1956c) The structure of chrysotile IV. Parachrysotile. Acta Crystallographica 9, 865-867.
Whittaker E.J.W. (1957) The structure of chrysotile V. Diffuse reflections and fibre texture. Acta Crystallographica 10, 149-156.
Yada K. (1967) Study of chrysotile asbestos by a high resolution electron microscope. Acta Crystallographica 23, 704-707.
Yada K. (1971) Study of microstructure of chrysotile asbestos by high resolution electron microscopy. Acta Crystallographica A27, 659-664.